



First In Situ Measurements of Electron Density and Temperature from Quasi-thermal Noise Spectroscopy with *Parker Solar Probe*/FIELDS

Michel Moncuquet¹, Nicole Meyer-Vernet¹, Karine Issautier¹, Marc Pulupa², J. W. Bonnell², Stuart D. Bale^{2,3,4,5},
Thierry Dudok de Wit⁶, Keith Goetz⁷, Léa Griton^{1,8}, Peter R. Harvey², Robert J. MacDowall⁹,
Milan Maksimovic¹, and David M. Malaspina¹⁰

¹ LESIA, Observatoire de Paris, Université PSL, CNRS, Sorbonne Université, Université de Paris, 5 place Jules Janssen, F-92195 Meudon, France
michel.moncuquet@obspm.fr

² Space Sciences Laboratory, University of California, Berkeley, CA 94720-7450, USA

³ Physics Department, University of California, Berkeley, CA 94720-7300, USA

⁴ The Blackett Laboratory, Imperial College London, London, SW7 2AZ, UK

⁵ School of Physics and Astronomy, Queen Mary University of London, London E1 4NS, UK

⁶ LPC2E, CNRS and University of Orléans, Orléans, France

⁷ School of Physics and Astronomy, University of Minnesota, Minneapolis, MN 55455, USA

⁸ IRAP, Université Toulouse III—Paul Sabatier, CNRS, CNES, Toulouse, France

⁹ Solar System Exploration Division, NASA/Goddard Space Flight Center, Greenbelt, MD 20771, USA

¹⁰ Laboratory for Atmospheric and Space Physics, University of Colorado, Boulder, CO 80303, USA

Received 2019 September 19; revised 2019 November 8; accepted 2019 November 20; published 2020 February 3

Abstract

Heat transport in the solar corona and wind is still a major unsolved astrophysical problem. Because of the key role played by electrons, the electron density and temperature(s) are important prerequisites for understanding these plasmas. We present such in situ measurements along the two first solar encounters of the *Parker Solar Probe*, between 0.5 and 0.17 au from the Sun, revealing different states of the emerging solar wind near the solar activity minimum. These preliminary results are obtained from a simplified analysis of the plasma quasi-thermal noise (QTN) spectrum measured by the Radio Frequency Spectrometer (FIELDS). The local electron density is deduced from the tracking of the plasma line, which enables accurate measurements, independent of calibrations and spacecraft perturbations, whereas the temperatures of the thermal and suprathermal components of the velocity distribution, as well as the average kinetic temperature, are deduced from the shape of the plasma line. The temperature of the weakly collisional thermal population, similar for both encounters, decreases with the distance as $R^{-0.74}$, which is much slower than adiabatic. In contrast, the temperature of the nearly collisionless suprathermal population exhibits a virtually flat radial variation. The 7 s resolution of the density measurements enables us to deduce the low-frequency spectrum of compressive fluctuations around perihelion, varying as $f^{-1.4}$. This is the first time that QTN spectroscopy is implemented with an electric antenna length not exceeding the plasma Debye length. As *PSP* will approach the Sun, the decrease in the Debye length is expected to considerably improve the accuracy of the temperature measurements.

Unified Astronomy Thesaurus concepts: Solar wind (1534); Space probes (1545); Plasma astrophysics (1261); Space plasmas (1544); Radio spectroscopy (1359); Space vehicle instruments (1548)

1. Introduction

The *Parker Solar Probe* (*PSP*) spacecraft (Fox et al. 2016), launched on 2018 August 12, is orbiting the Sun on highly elliptical trajectories of perihelion gradually decreasing from 35.7 solar radii (R_{\odot}) to the closest approach of 9.86 R_{\odot} from the center of the Sun, via Venus gravity assists. The present paper deals with the two first encounters that took place in 2018 October–November (E01) and 2019 March–April (E02), close to the heliographic equator, with perihelions of 0.17 au (35.7 R_{\odot}), therefore largely extending inward the *Helios* exploration. The trajectory crossed several times the heliospheric current sheet, thus revealing different types of wind and dynamic structures (Bale et al. 2019). During the so-called encounter phases of the trajectory, inward of 0.25 au (54 R_{\odot}), all instruments record data at a high rate (7 s cadence). In order to increase the radial extension of the results, we have also analyzed data farther away from the Sun, up to about 100 R_{\odot} (0.46 au), despite the reduced rate (56 s cadence).

Our results are based on power spectra acquired by the low-frequency receiver (LFR) of the Radio Frequency Spectrometer (RFS), which is a part of the FIELDS instrument suite on *PSP*

(Bale et al. 2016). The RFS instrument (Pulupa et al. 2017) is a two-channel receiver and spectrometer, at the terminals of four 2 m monopole electric antennas mounted near the front of the spacecraft close to the extremities of the heat shield diagonals, so that the two corresponding linear dipoles are 7 m tip-to-tip in length and are perpendicular to the axis of the spacecraft. The present preliminary results are based on data from only one dipole (V_1 – V_2). The LFR (10.5 kHz–1.7 MHz) spectra are analyzed with the technique of quasi-thermal noise (QTN) spectroscopy, which yields the electron density and the temperatures of the thermal (core) and suprathermal components of the velocity distribution, as well as the total kinetic temperature (e.g., Meyer-Vernet et al. 2017 and references therein).

The radial temperature profiles have never been measured in situ inward of 0.3 au. *Helios I* and *II*—from 0.3 to 1 au—and *Ulysses*—from about 1 to 4 au—found approximate power-law decreases with the distance of indices typically between -0.3 and -0.9 for the thermal core, with a flatter gradient for fast streams (Sittler & Scudder 1980; Pilipp et al. 1990; Phillips et al. 1995a; Issautier et al. 1998, 1999a; Maksimovic et al. 2000). The suprathermal

part, which includes a beaming component aligned to the magnetic field (also known as Strahl), was previously found to represent 4%–10% of the distribution (McComas et al. 1992; Štverák et al. 2009) and was found to have a temperature decreasing weakly with the distance (Phillips et al. 1995b; Pierrard et al. 2016).

Despite decades of study, the turbulence in the solar wind is still not fully understood, especially the role of compressive fluctuations in the transport of energy in a weakly collisional plasma. A question of considerable importance is the relationship between the small-scale structure associated with density fluctuations and large-scale plasma properties (Alexandrova et al. 2013; Lacombe et al. 2014; Lion et al. 2016). The accurate electron density samples obtained from QTN on *PSP* at perihelion enable us to study these compressive fluctuations much closer to the Sun than previously possible (Celnikier et al. 1983; Marsch & Tu 1990; Šafránková et al. 2015).

This paper is organized as follow. Section 2 recalls the main properties of QTN under *PSP* conditions and gives complete radio spectrograms for both solar encounters. Section 3 presents the methods to deduce the electron density and temperatures with some analytical approximations. Section 4 shows the radial variations of the electron thermal and suprathermal temperatures during the two first extended encounters and discusses the results and produces statistics. Section 5 uses the electron density data sets around $35.7 R_{\odot}$ to deduce the low-frequency spectrum of compressive fluctuations. Final remarks as conclusions are given in Section 6.

2. QTN Spectroscopy

Plasma particle properties in space are classically measured in situ by particle analyzers, pioneered in the solar wind by the “solar plasma experiment” on board Mariner 2 that provided (more than half a century ago; Neugebauer & Snyder 1962; Neugebauer 1997) the ultimate proof that this supersonic wind was more than a mere theoretician’s dream (Parker 1958, 2001).

In contrast, the technique of QTN spectroscopy measures particles via electrostatic fields, exploiting the strong coupling between plasma particles and fields (Sitenko 1967). Introduced on board the *International Sun-Earth Explorer-3* (Meyer-Vernet 1979) and pioneered to measure the cold (Meyer-Vernet et al. 1986a) and hot (Meyer-Vernet et al. 1986b) electrons in the tail of a comet, this technique uses the power spectrum of the voltage induced on an electric antenna by the particle quasi-thermal motions, measured by a radio receiver connected to an electric antenna. The signature of the electrons is a line at the electron plasma frequency, f_p , which reveals the total electron density, $n \propto f_p^2$, whereas the shape of the line reveals the electron kinetic temperature, as well as its thermal (core) and suprathermal components (Meyer-Vernet et al. 2017 and references therein).

The f_p plasma line is produced by Langmuir waves induced by the particle quasi-thermal motions. Since the Langmuir wavelength, λ_L , exceeds the ambient Debye length, L_D , the detection requires an electric antenna of a length exceeding L_D . However, electrons interact with waves of a phase speed equal to their proper speed, and since $\lambda_L \rightarrow \infty$ as the frequency $f \rightarrow f_p$, so does the Langmuir wave phase speed. Hence, suprathermal electrons can increase considerably the spectral density at f_p , producing a peak of amplitude characteristic of them (Meyer-Vernet & Perche 1989). On the other hand, the electrons passing by the antenna closer than L_D induce transient

voltages of duration $1/f_p$, which thus produce a flat spectrum for $f < f_p$, characteristic of the thermal core of the electron velocity distribution. Furthermore, the high-frequency spectrum is proportional to the total electron pressure.

Because $\lambda_L \rightarrow \infty$ as $f \rightarrow f_p$, the technique is equivalent to a detector of a large cross section—much larger than that of conventional spaceborne detectors—and it is relatively immune to spacecraft perturbations, photoelectrons, and charging effects (Meyer-Vernet et al. 1998). For these reasons, QTN spectroscopy is complementary to particle analyzers, serving routinely to calibrate them (e.g., Maksimovic et al. 1995; Issautier et al. 2001; Salem et al. 2001), and has been and will be implemented on a number of spacecraft in various environments (see, e.g., Moncuquet et al. 2009).

These properties are especially suitable on *PSP* because near the Sun, the 2 m electric antennas will be adequately longer than L_D , whereas the expected complex environment of the spacecraft (Ergun et al. 2010) will require a technique immune to spacecraft perturbations in order to measure the genuine plasma particle properties. However, the perihelion of the first *PSP* orbits, lying outward of $35 R_{\odot}$, is not close enough to the Sun for the Debye length to be smaller than the antenna length, which was unfortunately restricted by spacecraft safety considerations. Nevertheless, the suprathermal electrons, of a speed close to the phase speed of Langmuir waves near f_p , enables the plasma line to emerge (Figure 1).

3. Deducing the Electron Density and Temperatures

The electron density and temperatures are usually obtained from the QTN technique by assuming a model for the velocity distribution, calculating the theoretical QTN power spectral density, and deducing the parameters of the model by fitting the theory to the observations (e.g., Issautier et al. 1998). However, for the present preliminary results, we used a simpler method, based on simplified estimates of the relevant parts of the spectrum, similar to the method used on *Cassini* in Saturn’s magnetosphere (Moncuquet et al. 2005; Schippers et al. 2013); albeit at Saturn, the Debye length was short compared to the antenna length, whereas the opposite is true for these two first encounters (see Figure 2). Instead of using the whole spectra in the LFR–RFS frequency range with the model fitting, we determine the electron density from the frequency of the detected peak and the temperatures of thermal and suprathermal components of the electron distribution from the power level reached at the peak and the minimum level below the peak.

3.1. Electron Density

First of all, the local electron density is deduced from the tracking of the plasma line at f_p (see an example in Figure 7), with elimination of questionable measurements. Miscellaneous algorithms may be used for tracking the plasma line from the raw power spectrum at the inputs of the receiver, without any calibration, and a software to do so is implemented in RFS/FIELDS (Pulupa et al. 2017). In the present study, we use instead the algorithm developed for the Spectroscopie Ondes & Bruit Electrostatique Thermique radio receiver (Moncuquet et al. 2006; Kasaba et al. 2019) on the *BepiColombo* mission (European Space Agency & Japan Aerospace eXploration Agency (ESA-JAXA)), which is mainly based on detecting the steepest growth rate in each raw spectrum. This algorithm (somewhat improved for LFR–RFS) is efficient; for example,

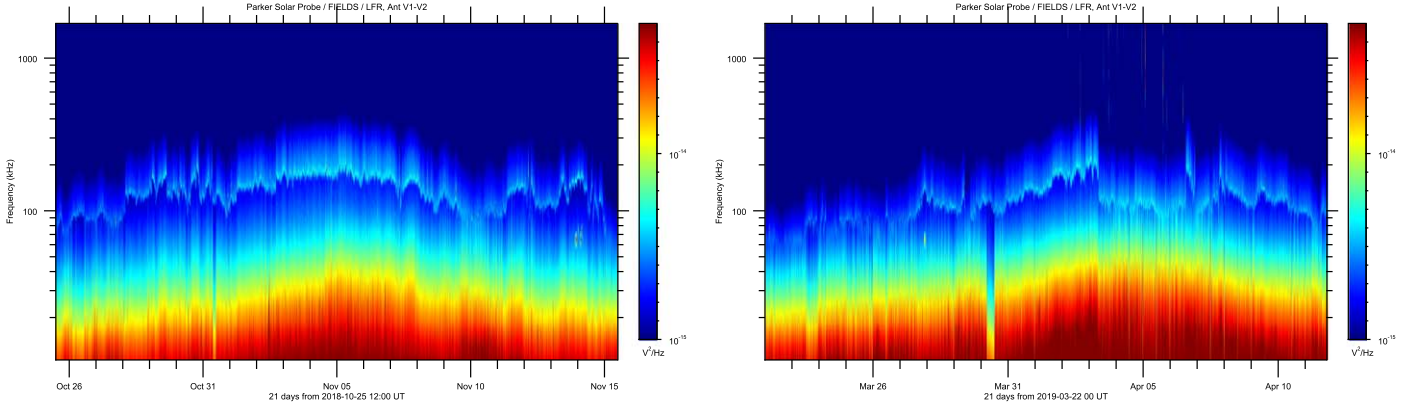


Figure 1. Twenty-one days spectrograms acquired during the first (2018 October 25–November 15, left panel) and second (2019 March 22–April 11, right panel) PSP solar encounters, showing the plasma quasi-thermal noise on which the plasma line at f_p emerges clearly (cyan line varying between 80 and 200 kHz).

during the high-rate data period in the first encounter (E01), the peak is detected in 95% of the available spectra ($\sim 130,000$ spectra). The main improvement of the algorithm was to withdraw the false positives (for example, with type III bursts or strong interferences). We used the fact that a supposedly high f_p must provide a relative high peak level if it is bona-fide QTN (since the peak behaves roughly as $\sqrt{f_p}$, see Equation (2) below); otherwise, the detection is withdrawn. This represents about 2% of the initial selection (3% for the second encounter, likely because of the numerous type III bursts and the dilute wind around perihelion).

The deduced electron density is plotted (black dots) on Figure 2. Because they stem from a detection algorithm (instead of a model fitting), these results are stepped since LFR–RFS uses only 64 pseudo-logarithmically spaced frequencies in the range of 10 kHz–1.7 MHz. As a consequence, the lowest densities (say $< 100 \text{ cm}^{-3}$) are more stepped than the higher ones, with larger error bars.

3.2. Electron Temperatures

1. The temperature, T_c , of the thermal component of the velocity distribution, assumed to be Maxwellian, is then deduced from the voltage spectral density just below f_p , hereafter noted as V_{\min}^2 (see Figure 7). This quantity is essentially the plateau QTN spectrum, hereafter noted as V_0^2 , and is produced by electrons passing around the antennas closer than L_D on which the effect of the separation of the antenna arms is discussed in the Appendix A. To calculate V_0^2 at the receiver inputs, one must take into account the antenna gain calculated from the load/stray capacitance and the impedance of the antenna modified by the plasma. The QTN plateau is then given as a function of the core temperature, T_c , and the Debye length, L_D , by (from Moncuquet et al. 2005)

$$V_0^2 \approx \frac{8\sqrt{2m_e k_B T_c}}{\pi^{3/2} \epsilon_0 (1 + C_B/C_A)^2} \int_0^\infty \frac{F(kL) k L_D^2}{[k^2 L_D^2 + 1]^2} dk \quad (1)$$

in S.I. units, V_0^2 being in V^2/Hz . Here, $F(kL)$ is the PSP wire antenna response (detailed in Appendix A), with L as the single wire length ($L \simeq 2 \text{ m}$); $C_A = \pi \epsilon_0 L / \ln(L_D/a)$ is an approximation of the dipole antenna capacitance at low frequencies, with a as the wire radius ($a \simeq 1.5 \text{ mm}$); and C_B is the (dipole) stray capacitance ($\sim 18 \text{ pF}$). Two

(generally minor) contributions must be added to this plateau QTN: the shot noise, V_{shot}^2 , produced by the currents flowing between the antennas and the plasma, possibly mitigated/enhanced by the antenna biasing, and the Doppler-shifted protons, QTN V_p^2 . Finally, we use an iterative method to solve the implicit Equation (1) and deduce T_c from the observable V_{\min}^2 , taking into account at each step some approximations of V_{shot}^2 and V_p^2 (see Appendix B).

The deduced core temperature, T_c , during the first (top) and second (bottom) extended solar encounters is plotted in blue in Figure 2. The vertical dashed lines indicate the beginning and end of the high-rate data (7 s). The vertical dotted lines indicate a period when the data are perturbed by biasing or a change in modes; this is unfortunate because this day is one of the rare periods of high wind speed in E01, therefore preventing us from measuring the thermal electron properties in high speed wind.

2. The temperature of the suprathermal component of the velocity distribution is obtained using the ratio V_{\max}^2 / V_{\min}^2 between the peak level and the level V_{\min}^2 (see Figure 7), and is, therefore, independent of calibration or biasing that affect the two levels in the same way. Statistically, this ratio is well centered with regular variance. Modeling the suprathermal electrons by a Kappa distribution (which includes the Maxwellian case $\kappa \rightarrow \infty$), the peak level may be estimated using Equations (59)–(60) from Meyer-Vernet et al. (2017; with range of validity therein, including the case $L_D > L$). We deduce the following estimate for the temperature T_h of the suprathermal electrons:

$$\frac{V_{\max}^2}{V_{\min}^2} \approx \frac{\kappa - 3/2}{\kappa} \frac{F(A L/L_D)}{F_0(L/L_D)} \sqrt{\frac{\pi f_p}{12 \Delta f}} \frac{T_h}{\sqrt{T_c T}}, \quad (2)$$

where Δf is the frequency resolution of the instrument at the plasma frequency, f_p ; T is the electron kinetic temperature, $A \simeq \sqrt{T_c/T} \sqrt{2\Delta f/3f_p}$; and F_0 is the value of the integral in Equation (1) (also detailed in Appendix A).

Given the uncertainties on the whole electron velocity distribution and the approximations made in our QTN modeling, which presently does not take into account the anisotropy of the Strahl, we will only exploit the centered estimator V_{\max}^2 / V_{\min}^2 obtained from the data,

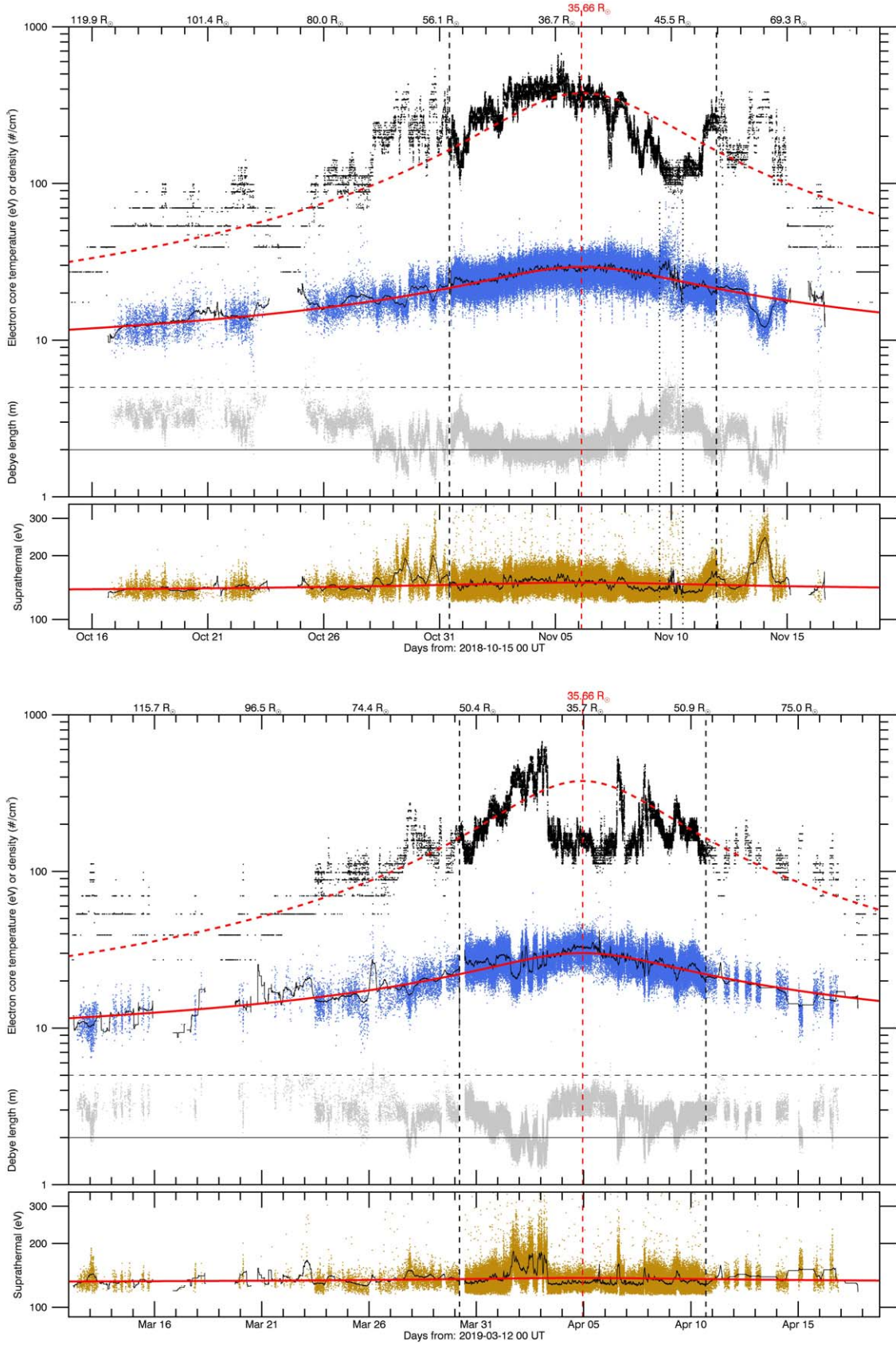


Figure 2. Electron total density (black, in cm^{-3} , with an arbitrary $10 \times R_{\text{AU}}^{-2}$ variation superimposed in red) and temperatures (in eV, with the fitted radial variations shown in Figure 3 superimposed in red) of the thermal (core, in blue) and suprathermal (in gold) components of the electron velocity distribution for the first (2018 October 15–November 18, top panel) and second (2019 March 12–April 18, bottom panel) extended encounters. The solid black line over the T_c and T_h values is a one-hour smoothing. The corresponding plasma Debye length (m) is plotted in gray (compared to the 2 m antenna length in black). The heliocentric distance (in the Sun radius) is indicated at the top of each panel (in red for each *PSP* perihelion).

without trying to match a value of κ . In other words, we deduce a proxy T_h of the temperature of the suprathermal component of the distribution assuming merely $T_h \propto V_{\max}^2/V_{\min}^2$ and using Equation (2) to dimensionate, with $\kappa = 5$. These temperatures are plotted in gold at the bottom of Figure 2 for the first (top) and second (bottom) extended solar encounters. Note that the results for different values of κ can be deduced from Equation (2); for example, with Maxwellians, T_h would be 30% smaller.

3. The electron kinetic temperature, T , is deduced from the high-frequency part of the spectrum. For antennas long enough with respect to L_D , the high-frequency QTN varies as f^{-3} and is directly proportional to the kinetic temperature and is independent of the separation between the antenna arms (Meyer-Vernet & Perche 1989); a result independent of the velocity distribution provided it is isotropic (Chateau & Meyer-Vernet 1991). However, for the first and second *PSP* orbits, the Debye length is not small enough, so the kinetic temperature can be estimated from fitting the high-frequency part of the spectrum, after subtraction of the galactic noise and the receiver noise (Maksimovic et al. 2019). Note that, contrary to the determination of T_c , such a simplified method cannot be implemented in the presence of electromagnetic emissions, which were frequent during encounter E02 (Pulupa et al. 2020); it is also much less accurate than if obtained by fitting the whole spectrum, since at high frequencies, the QTN is of the same order of magnitude as the receiver noise and the galactic noise.

4. Large-scale Variations

4.1. Radial Profiles of Electron Temperatures

Figure 3 shows the thermal (core, in blue) and suprathermal (in gold) electron temperatures as a function of heliocentric distance R in units of solar radius R_\odot , with the fitted power laws (in red) given by

$$\begin{aligned} T_{c(\text{eV})} &\simeq 418 \times (R/R_\odot)^{-0.74} \\ \times T_{h(\text{eV})} &\simeq 185 \times (R/R_\odot)^{-0.06} \quad \text{for E01} \end{aligned} \quad (3)$$

$$\begin{aligned} T_{c(\text{eV})} &\simeq 432 \times (R/R_\odot)^{-0.74} \\ \times T_{h(\text{eV})} &\simeq 153 \times (R/R_\odot)^{-0.03} \quad \text{for E02} \end{aligned} \quad (4)$$

for the first and second extended encounters, respectively. Note that these results are obtained using robust straight-line fits, i.e., minimizing the mean absolute deviation. From its value, we estimate an error on the logarithmic slopes of the profiles of about ± 0.03 .

Both extended encounters have similar temperature profiles despite the differences in densities. The thermal temperature is about 3.5×10^5 K at $36 R_\odot$ (0.17 au) and 2.3×10^5 K at $64 R_\odot$ (0.3 au). The latter value and the radial profile are similar to those found by *Helios* (Pilipp et al. 1990; Maksimovic et al. 2005), despite the general decrease in solar activity until the *Helios* epoch and the expected overall decrease in coronal temperature (Schwadron et al. 2014). In contrast, the radial profile of the suprathermal electron temperature is nearly flat. The flatness of T_h agrees with the *Helios* results inward of 1 au (Maksimovic et al. 2005; Pierrard et al. 2016), but the absolute values are somewhat higher (1.6 million degrees at $64 R_\odot$

(0.3 au)). This might be due to the crudeness of our T_h measurements (see Section 3), for which the logarithmic slope of the T_h profile is more accurate than the absolute values. However, extrapolating to $1.5 R_\odot$ yields a temperature of $(1.7\text{--}2.1) \times 10^6$ K, which is in the range of electron temperatures measured in the quiet corona (David et al. 1998) and in streamers at the solar activity minimum (Kohl et al. 1997; Gibson et al. 1999).

4.2. Discussion

With the density and core temperature measured at 0.17 au, the mean free path of thermal electrons is of the same order of magnitude of the pressure scale height, i.e., their Knudsen number is of order of magnitude unity. Under such weakly collisional conditions, the heat flux is not given by the Spitzer–Härm value, whose validity requires a much smaller Knudsen number (Scudder & Olbert 1979; Shoub 1983), but collisions are not negligible, requiring numerical kinetic simulations. Such simulations, taking into account Coulomb collisions, spherical expansion with a radial magnetic field, and the electrostatic field produced by the electron–proton mass difference being computed self-consistently, yield a thermal electron temperature that decreases with the distance with a logarithmic slope in the range of 0.6–0.9 and an antisunward drifting suprathermal component, which tends to have an isothermal profile (Landi et al. 2012).

This nearly isothermal behavior of suprathermal electrons, with a nearly constant relative density of a few times $(m_e/m_p)^{1/2}$ (m_e and m_p being the electron and proton masses) were predicted by Meyer-Vernet & Issautier (1998) using an analytical approximation of an exospheric solar wind model (Lemaire & Scherer 1971) with a radial magnetic field. The constant kinetic temperature of suprathermal electrons is a simple consequence of conservation of energy and magnetic momentum for electrons escaping from the solar electrostatic potential and is consistent with an adiabatic anisotropic fluid behavior, whereas the value of the relative density comes from the equality of electron and proton densities and escaping fluxes. The suitability of exospheric models for suprathermal electrons is due to the increase in the Coulomb free path as the square of the energy, making them collisionless. This assumes that if instabilities (Marsch 2006) and scattering by turbulent fluctuations at electronic scales change the velocity directions, they also negligibly change the kinetic energy per particle of this component of the distribution. However, as expected, this agreement does not hold for the collisional thermal electrons, for which exospheric theory predicts an adiabatic radial variation with a logarithmic slope of $-4/3$, as a consequence of their trapping by the solar electrostatic potential (Meyer-Vernet et al. 2003). The weaker observed slope is presumably due to the heat flux carried by the suprathermal electrons, which decreases radially faster than R^{-2} (Scime et al. 2001), implying heat deposition in the plasma. A more detailed comparison should take into account that our measurements of T_c and T_h concern the temperatures of the two untruncated components of the velocity distribution, whereas the exospheric distinction between populations involves truncations in velocity space.

Finally, from the relation $T = T_c + (n_h/n) \times T_h$, where T is the electron kinetic temperature; T_c and T_h are those of the thermal (core) and suprathermal component of the distribution, respectively; and n_h/n is the relative density of the

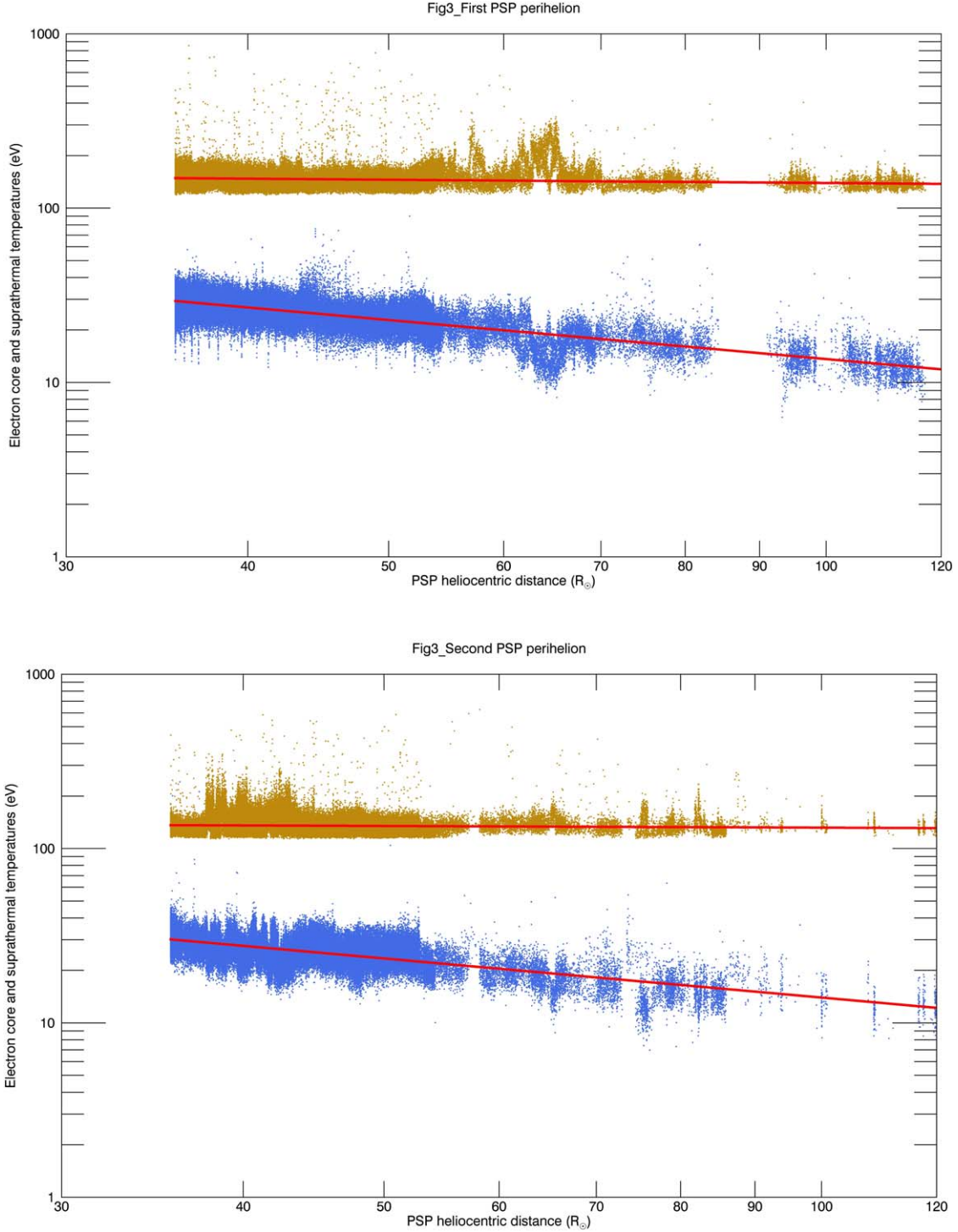


Figure 3. Variation with the heliocentric distance of the temperatures of the thermal (core, in blue) and suprathermal (in gold) components of the electron velocity distribution for the extended E01 (top) and E02 (bottom), with the fitted profiles superimposed in red.

suprathermals, assumed to be about 10% from *Helios* measurements (Štverák et al. 2009). We obtain $T \simeq 5 \times 10^5$ K at 0.17 au, which is in agreement with the high-frequency QTN (Maksimovic et al. 2020).

4.3. Statistics of the Electron Density and Core Temperature during E01 and E02

Most of the large-scale differences in density between E01 and E02 that are apparent in Figure 2 do not seem to have

counterparts in the electron thermal temperatures. To examine this point, below we use our large data set to study the different regimes encountered.

The top panels of Figure 4 represent the histograms of the electron density ($\sim 115,000$ data points) and the core electron temperature ($\sim 112,500$ data points) during the first encounter E01, i.e., 2018 October 31 to November 11, with a 7 s resolution (solid line histograms). We normalize each histogram to 0.17 au, using an R^{-2} density dependence and the $R^{-0.74}$ power law

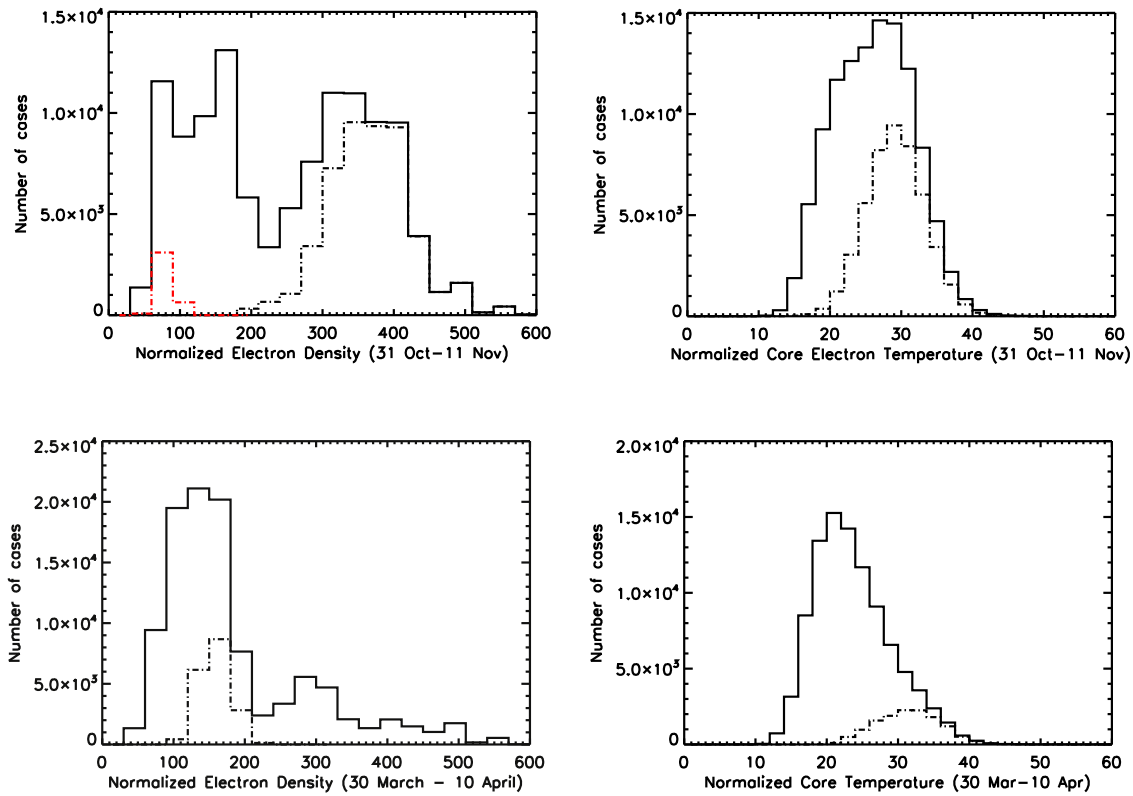


Figure 4. Histograms of the electron density (left) and the core (thermal) electron temperature (right) for both encounters. For E01 in the top panels, we superimpose a dilute wind period (November 9–10) as a red dotted–dashed line and a period of dense wind (gray distribution) around the first perihelion (November 3–6). For E02 in the bottom panels, we overplot a dotted–dashed gray line as the histogram of density and temperature measured around the second perihelion (2019 April 3–6).

determined in Section 4 for T_c . During the approach to E01, *PSP* showed a complex solar wind structure with different regimes, i.e., slow and intermediate wind from streamers and flow interactions, in addition to sporadic faster flows from small equatorial coronal holes, which are typical of equatorial regions (Phillips et al. 1995c; Issautier et al. 1998, 2005; Neugebauer 2001). For E01, the electron density histogram exhibits two main kinds of populations: a dilute electron population (with a mean value $\simeq 130 \text{ cm}^{-3}$ at $35.7 R_\odot$) and a dense electron population (with a mean value $\simeq 330 \text{ cm}^{-3}$). We superimpose a gray dotted–dashed histogram obtained during E01, from 2018 November 3–6; we do see that this period mainly contains a denser wind population with a mean value of $\sim 370 \text{ cm}^{-3}$. The red dotted–dashed histogram is obtained midday on 2018 November 9–11, where a faster solar wind is measured (Kasper et al. 2019). We can thus attribute the most dilute electron distribution to the fastest wind, which is in agreement with the well-known anticorrelation between the solar wind density and speed (Neugebauer 2001). In contrast, the shape of the core electron temperature histogram shows mainly one single population for E01. It has a mean value of 26 eV, whereas the gray dotted–dashed core temperature has a mean around 29 eV. Contrary to the electron density, the core temperature is more difficult to associate to specific structures. In particular, many interplanetary events from denser populations could be correlated with the same kind of temperature distributions (Salem et al. 2003).

We have also plotted the distributions of the scaled electron density ($\sim 120,000$ data points) and core temperature ($\sim 105,000$ data points) at 0.17 au for E02 in the bottom panels of Figure 4. We normalize each histogram to 0.17 au as we did for E01. The density populations are likely to be associated with three major

classes of solar wind: the quiet undisturbed wind with lower mean values of density $\simeq 120 \text{ cm}^{-3}$, which dominates for E02; the denser heliospheric plasma sheet with intermediate values of density ($\simeq 290 \text{ cm}^{-3}$); and the overdense disturbed wind with interplanetary shocks, density compressions regions, etc., with higher mean values of density ($\simeq 400 \text{ cm}^{-3}$). Note that these mean values correspond to those obtained at 1 au, but shifted to $35.7 R_\odot$. The gray dotted–dashed histogram is obtained from 2019 April 3–6, where the density is 50% smaller than the one obtained during E01, i.e., $\simeq 160 \text{ cm}^{-3}$. The corresponding core temperature has a mean value around 31.5 eV. We can conclude that for this period, the dilute density is correlated to the highest core electron temperature. Future works will need a detailed study on the large-scale structure of the wind, using in particular the wind speed data.

5. Low-frequency Compressive Turbulence in the Pristine Solar Wind

The 7 s resolution of the density measurements obtained by the QTN analysis on *PSP* enables us to deduce the spectrum of compressive fluctuations at $\sim 36 R_\odot$, during the two first encounters. To analyze the electron density fluctuations, we use the Morlet wavelet transforms, which are convenient for unfolding turbulence signals into both space (or time) and scale (Farge 1992). Figure 5 shows the spectrum of the electron density fluctuations, normalized to the corresponding mean density value, for each perihelion where the radial distance is almost constant, close to 0.17 au. Spectra vary as an $f^{-1.4}$ power law (blue solid line) in the 10^{-4} – 10^{-2} Hz frequency range, which is in agreement with some previous analyses in this frequency range at 1 au (Intriligator 1975; Issautier et al. 2010; Roberts et al. 2017). For E01, from 2018 November 3–6, the density measurements (see Figures 2 and 4) of

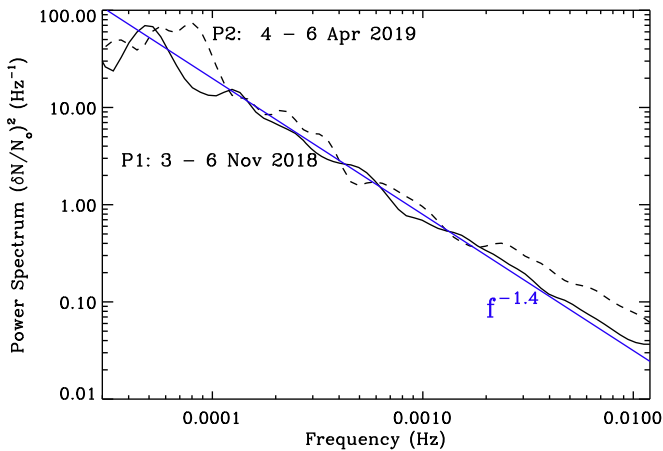


Figure 5. Normalized power spectrum of density fluctuations obtained at $\sim 36 R_{\odot}$, for both E01 (solid line) and E02 (dashed line). The blue solid line shows the corresponding power-law spectrum, varying as $f^{-1.4}$.

the mean value at $\sim 370 \text{ cm}^{-3}$ suggest a low speed wind stream (Kasper et al. 2019). In contrast, for E02, from 2019 April 4–6, the plasma is more dilute with a mean density of $\sim 160 \text{ cm}^{-3}$ (see Section 4.3). Although *PSP* explores different types of wind in E01 and E02, the corresponding amplitude of the normalized power spectrum of the electron density is similar, around 1 at 10^{-3} Hz . However, at higher frequencies, i.e., above $2 \times 10^{-3} \text{ Hz}$, the amplitude of the spectrum is twice as high for E02 than for E01. We have checked that the enhancement of this part of the spectrum corresponds to the electron density structure of 2019 April 5 (see Figure 2), coming from the fastest solar wind stream, with Alfvénic turbulent fluctuations (Kasper et al. 2019). Hence, this dilute solar wind has a higher level of turbulence fluctuations.

A detailed study of the 3D structure of the turbulence needs, in particular, to correlate the density spectrum with macroscopic plasma parameters; radial distances; values of the plasma, β ; and local magnetic field switch back fluctuations, which are outside the scope of this paper. As it approaches closer to the Sun, *PSP* will give new crucial clues.

6. Concluding Remarks

For these preliminary results on far solar encounters, QTN spectroscopy has been implemented in a simplified way, mainly due to the small antenna length, whereas the suprathermal electrons have been considered globally, neglecting their anisotropy. These simplifications did not affect the accuracy of the density measurements; concerning the temperatures, the present preliminary determinations of the radial profiles are expected to be more robust than the absolute values.

For both studied encounters, the radial profile of the temperature, T_c , of the thermal component varies as $R^{-0.74}$ with similar values at equal distances. These values are in the range of *Helios* measurements. The temperature T_h of the suprathermal component has a very weak radial variation, as expected from its virtually collisionless state, with extrapolated values at the corona compatible with previous coronal measurements close to the solar equator. As a by-product, the accurate determination of the electron density by the QTN enables us to deduce the low-frequency spectrum of compressive fluctuations around perihelion, varying as $f^{-1.4}$.

Future works will require a detailed study of the structure of the wind, using the parameters available, especially the magnetic field and the velocity. In particular, we intend to study the electron

density and temperature(s) behavior during the magnetic field reversals and jumps in speed (Bale et al. 2019) and to explore the relation between density and core temperature with radial distances. We will also exploit the measured electron temperature gradient to study the interplanetary potential and the heat transport.

Note that the present results have been obtained independently of those from the onboard electron analyzer of the Solar Wind Electrons Alphas and Protons instrument suite (Kasper et al. 2016; Halekas et al. 2020). Comparisons between the latter results and those from QTN spectroscopy should benefit to both techniques. Concerning QTN spectroscopy, we intend to model the suprathermal electrons by taking into account the anisotropy of the Strahl component and to implement the technique via fitting the whole QTN spectrum, when *PSP* will be close enough to the Sun for the Debye length to be smaller than the antenna length.

Parker Solar Probe was designed, built, and is now operated by the Johns Hopkins Applied Physics Laboratory as part of NASA’s Living with a Star (LWS) program (contract NNN06AA01C). Support from the LWS management and technical team has played a critical role in the success of the *Parker Solar Probe* mission. We warmly congratulate all the scientists, technicians, engineers, and administrators who contributed to this outstanding mission. This work is based on observations with the FIELDS instrument suite embarked on *Parker Solar Probe* whose data are publicly available at <http://fields.ssl.berkeley.edu/data/>. In France, this work was supported by CNES and by CNRS/INSU. We thank O. Alexandrova for helpful discussions. S.D.B. acknowledges the support of the Leverhulme Trust Visiting Professorship program.

Appendix A Antenna Arms Separation

The response $F(kL)$ of a dipole made of two collinear wires of length L with a gap of length s between the wires reads as (from Equation (32) by Meyer-Vernet & Perche 1989)

$$F(kL) = \frac{J_0^2(ka)}{2k^2 L^2} \{ k(L+s) \text{Si}(k(L+s)) + kL \text{Si}(kL) \\ - k(L+s/2) \text{Si}(k(2L+s)) - ks/2 \text{Si}(ks) \\ - 4 \sin^2(k(L+s)/2) \sin^2(kL/2) \} \quad (5)$$

(Si denotes the sine integral function and J_0 denotes the Bessel function of the order of 0). In particular, from the asymptotic values of $F(kL)$, an equivalent dipole wire length may be defined as $(L+s)$ for $kL \rightarrow 0$ and L for $kL \rightarrow \infty$.

The QTN plateau level V_0^2 given in Equation (1) depends on the response $F(kL)$, including the separation, s , via the integral over wavenumbers, k , noted as F_0 given by

$$F_0 = \int_0^\infty \frac{F(kL) k L_D^2}{[k^2 L_D^2 + 1]^2} dk. \quad (6)$$

Hence, the effect on the QTN plateau level may be calculated as a function of the dimensionless ratios L/L_D and s/L at each step of the algorithm used to derive the thermal electron temperature. When using the asymptotic values of $F(kL)$ sketched above, note that the effect of the wire separation on the QTN plateau level is equivalent to that produced by a wire length of $(L+s)$ for $L_D \gg L$, whereas for $L_D \ll L$ (which may

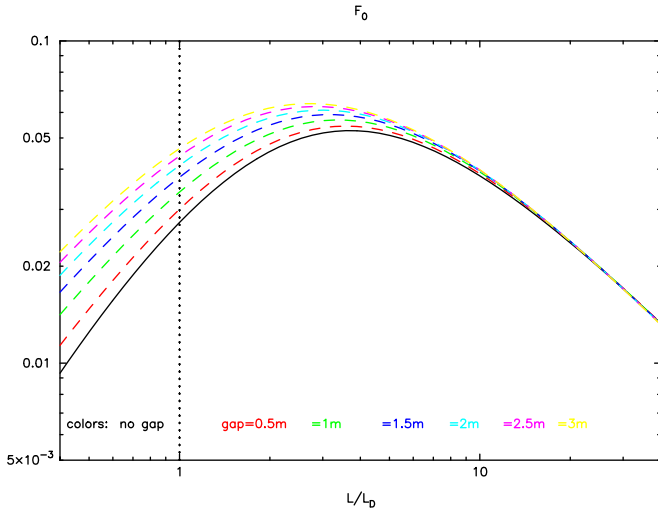


Figure 6. Effect of the separation of the antenna arms: QTN plateau in V^2/Hz with T_c in K, normalized to $8.14 \times 10^{-16} \sqrt{T_c}$ as a function of L/L_D with separation (dashed color lines) and without separation (continuous black line).

happen closer to the Sun), the separation effect will be negligible. The function F_0 is shown in Figure 6 as a function of L/L_D for different values of the separation in the range of [0–3]m.

On *PSP*, the physical separation between the antenna wires V1 and V2 is ~ 3 m but is alleviated by the presence of the spacecraft, so that the effective separation is much smaller. By fitting s in the range of [0–3]m with the algorithm used to solve the implicit Equation (1), we have empirically determined $s \sim 1.5$ m, so that, for large L_D and for frequencies below f_p , V1–V2 behaves as a dipole of 2×3.5 m.

Appendix B

The Simplified QTN Method and Other Noises

Figure 7 shows an example of implementation of the simplified QTN method (without fitting) to obtain the preliminary results reported in the present paper, based on

the plasma peak, f_p , and the minimum, V_{\min}^2 , and maximum, V_{\max}^2 , noise levels.

Dealing with shot and proton noises—As indicated in Section 3.2, the observed QTN minimum below f_p reads as $V_{\min}^2 = V_0^2 + V_{\text{shot}}^2 + V_p^2$, where the main contribution is the QTN plateau, V_0^2 , given by Equation (1). We focus here on the minor contributions arising from the shot noise, V_{shot}^2 , and the Doppler-shifted proton noise, V_p^2 , which are both varying as $\sqrt{T_c}$ but whose variation depends on unknown parameters that are the antenna direct current potential, ϕ , and, mainly, the wind bulk velocity, respectively:

- (1) The shot noise, including photoelectron, plasma, and bias currents, is detailed in Meyer-Vernet et al. (2017), with estimations for *PSP* in the case of $L_D \ll L$. Our simplified method computes the shot noise for any L_D (from Equation (2) by Moncuquet et al. 2005), assuming $\phi = 0$ and that antenna biasing yields a stable noise modifying V_{shot}^2 by a fixed factor. The ratio V_{shot}^2/V_0^2 has been confirmed to be less than 10% for both encounters. Note that we have kept all the available spectra for the first encounter, whereas for the second encounter, we have withdrawn the short (half-hour) periodic tests of unbiasing. That explains why, for the first encounter, we can see some periodic short (and unphysical) drops of T_c values in Figure 2 (top panel).
- (2) The QTN V_p^2 produced by the plasma protons, Doppler-shifted by the solar wind speed, and especially its variation with $\sqrt{T_c}$ for different values of L/L_D is given by Issautier et al. (1999b, Equation (22) and Figure 1 therein). With a wind speed varying from 200 to 400 km s^{-1} and with L/L_D between 0.5 and 2 (i.e., typical ranges for both encounters), this yields a ratio of $r = V_p^2/V_0^2$ less than 5% within these ranges. So, for each spectrum, we fit r in the range of [0–0.05] in our algorithm used to determine T_c . Finally, note that V_p^2 is expected to be negligible as *PSP* will approach the Sun (Meyer-Vernet et al. 2017, Section 2.8).

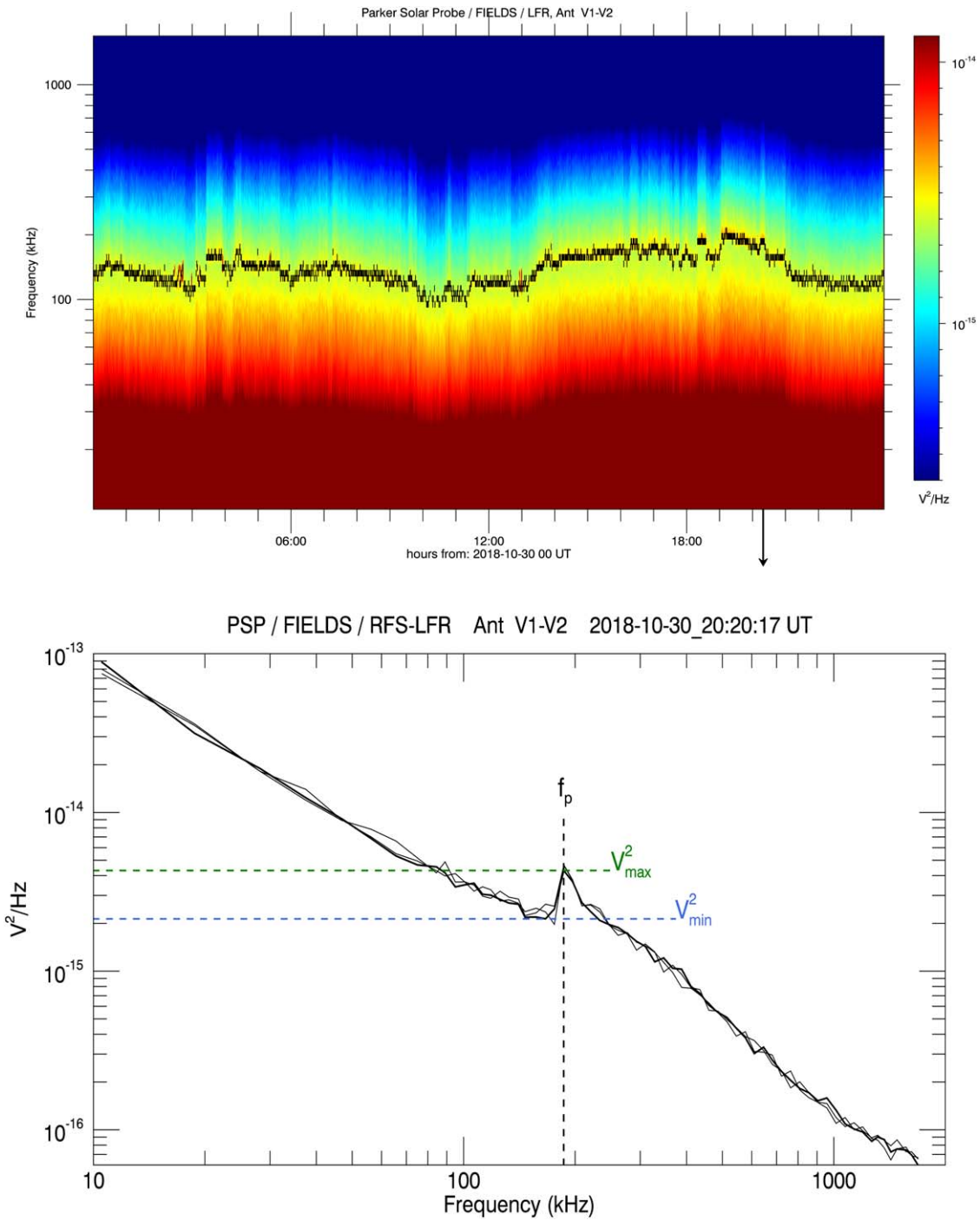


Figure 7. Top panel: example of a daily spectrogram (2018 October 30, 57 s acquisition cadence) in the LFR–RFS frequency range, with the detected plasma peaks, f_p , superimposed as black bars, which enables us to deduce the electron density. Bottom panel: example of three consecutive calibrated spectra (middle acquisition UT indicated on the top and by the arrow from the spectrogram time line), showing f_p and the two noise levels (dashed lines) used in this paper to determine the thermal and suprathermal temperatures.

ORCID iDs

Michel Moncuquet <https://orcid.org/0000-0002-9621-0365>
 Nicole Meyer-Vernet <https://orcid.org/0000-0001-6449-5274>
 Karine Issautier <https://orcid.org/0000-0002-2757-101X>
 Marc Pulupa <https://orcid.org/0000-0002-1573-7457>
 J. W. Bonnell <https://orcid.org/0000-0002-0675-7907>
 Stuart D. Bale <https://orcid.org/0000-0002-1989-3596>
 Thierry Dudok de Wit <https://orcid.org/0000-0002-4401-0943>

Keith Goetz <https://orcid.org/0000-0003-0420-3633>
 Léa Griton <https://orcid.org/0000-0001-8956-2824>
 Peter R. Harvey <https://orcid.org/0000-0002-6938-0166>
 Robert J. MacDowall <https://orcid.org/0000-0003-3112-4201>
 Milan Maksimovic <https://orcid.org/0000-0001-6172-5062>
 David M. Malaspina <https://orcid.org/0000-0003-1191-1558>

References

- Alexandrova, O., Chen, C. H. K., Sorriso-Valvo, L., et al. 2013, *SSRv*, **178**, 101
- Bale, S. D., Badman, S. T., Bonnell, J. W., et al. 2019, *Natur*, **576**, 237
- Bale, S. D., Goetz, K., Harvey, P. R., et al. 2016, *SSRv*, **204**, 49
- Celnikier, L., Harvey, C. C., Jegou, R., Moricet, P., & Kemp, M. 1983, *A&A*, **126**, 293
- Chateau, Y. F., & Meyer-Vernet, N. 1991, *JGR*, **96**, 5825
- David, C., Gabriel, A. H., Bely-Dubau, F., et al. 1998, *A&A*, **336**, L90
- Ergun, R. E., Malaspina, D. M., Bale, S. D., et al. 2010, *PhPI*, **17**, 072903
- Farge, M. 1992, *AnRFM*, **24**, 395
- Fox, N. J., Velli, M. C., Bale, S. D., et al. 2016, *SSRv*, **204**, 7
- Gibson, S. E., Fludra, A., Bagenal, F., et al. 1999, *JGR*, **104**, 9691
- Halekas, J. S., Whittlesey, P., Larson, D. E., et al. 2020, *ApJS*, doi:10.3847/1538-4365/ab4ccc
- Intriligator, D. S. 1975, *ApJ*, **196**, 879
- Issautier, K., Mangeney, A., & Alexandrova, O. 2010, in AIP Conf. Proc. 1216, 12th SOLAR WIND Conf., ed. M. Maksimovic et al. (Melville, NY: AIP), 148
- Issautier, K., Meyer-Vernet, N., Moncuquet, M., & Hoang, S. 1998, *JGR*, **103**, 1969
- Issautier, K., Meyer-Vernet, N., Moncuquet, M., & Hoang, S. 1999a, in AIP Conf. Proc. 471, SOLAR WIND 9, ed. S. R. Habbal et al. (Melville, NY: AIP), 581
- Issautier, K., Meyer-Vernet, N., Moncuquet, M., & McComas, D. J. 1999b, *JGR*, **104**, 15665
- Issautier, K., Perche, C., Hoang, S., et al. 2005, *AdSpR*, **35**, 2141
- Issautier, K., Skoug, R. M., Gosling, J. T., Gary, S. P., & McComas, D. J. 2001, *JGR*, **106**, 15665
- Kasaba, Y., Kojima, H., Moncuquet, M., et al. 2019, *SSRv*, submitted
- Kasper, J. C., Abiad, R., Austin, G., et al. 2016, *SSRv*, **204**, 131
- Kasper, J. C., Bale, S. D., Belcher, J. W., et al. 2019, *Natur*, **576**, 228
- Kohl, J. L., Noci, G., Antonucci, E., et al. 1997, *SoPh*, **175**, 613
- Lacombe, C., Alexandrova, O., Matteini, L., et al. 2014, *ApJ*, **796**, 5
- Landi, S., Matteini, L., & Pantellini, F. 2012, *ApJ*, **760**, 143
- Lemaire, J., & Scherer, M. 1971, *JGR*, **76**, 7479
- Lion, S., Alexandrova, O., & Zaslavsky, A. 2016, *ApJ*, **824**, 47
- Maksimovic, M., Bale, S. D., Berčič, L., et al. 2020, *ApJS*, doi:10.3847/1538-4365/ab61fc
- Maksimovic, M., Gary, S. P., & Skoug, R. M. 2000, *JGR*, **105**, 18337
- Maksimovic, M., Hoang, S., Meyer-Vernet, N., et al. 1995, *JGR*, **100**, 19881
- Maksimovic, M., Zouganelis, I., Chaufray, J., et al. 2005, *JGR*, **110**, A09104
- Marsch, E. 2006, *LRSP*, **3**, 1
- Marsch, E., & Tu, C. Y. 1990, *JGR*, **95**, 11945
- McComas, D. J., Bame, S. J., Feldman, W. C., Gosling, J. T., & Phillips, J. L. 1992, *GeoRL*, **19**, 1291
- Meyer-Vernet, N. 1979, *JGR*, **84**, 5373
- Meyer-Vernet, N., Couturier, P., Hoang, S., et al. 1986a, *Sci*, **232**, 370
- Meyer-Vernet, N., Couturier, P., Hoang, S., Perche, C., & Steinberg, J. L. 1986b, *GeoRL*, **13**, 279
- Meyer-Vernet, N., Hoang, S., Issautier, K., et al. 1998, *GMS*, **103**, 205
- Meyer-Vernet, N., & Issautier, K. 1998, *JGR*, **103**, 29705
- Meyer-Vernet, N., Issautier, K., & Moncuquet, M. 2017, *JGR*, **122**, 7925
- Meyer-Vernet, N., Mangeney, A., Maksimovic, M., Pantellini, F., & Issautier, K. 2003, in AIP Conf. Proc. 679, 10th SOLAR WIND Conf., ed. M. Velli et al. (Melville, NY: AIP), 263
- Meyer-Vernet, N., & Perche, C. 1989, *JGR*, **94**, 2405
- Moncuquet, M., Lecacheux, A., Meyer-Vernet, N., Cecconi, B., & Kurth, W. S. 2005, *GeoRL*, **32**, L20S02
- Moncuquet, M., Matsumoto, H., Bougeret, J. L., et al. 2006, *AdSpR*, **38**, 680
- Moncuquet, M., Mayer-Vernet, N., Bougeret, J.-L., et al. 2009, in AIP Conf. Proc. 1144, Future Perspectives of Space Plasma and Particle Instrumentation, ed. M. Hirahara et al. (Melville, NY: AIP), 59
- Neugebauer, M. 1997, *JGR*, **102**, 26887
- Neugebauer, M. 2001, in The Heliosphere near Solar Minimum, ed. A. Balogh, R. G. Marsden, & E. J. Smith (London: Springer), 43
- Neugebauer, M., & Snyder, C. W. 1962, *Sci*, **138**, 1095
- Parker, E. N. 1958, *ApJ*, **128**, 664
- Parker, E. N. 2001, in The Century of Science, ed. J. A. M. Bleeker, J. Geiss, & M. C. E. Huber (New York: Kluwer), 225
- Phillips, J. L., Bame, S. J., Barnes, A., et al. 1995c, *GeoRL*, **22**, 3301
- Phillips, J. L., Bame, S. J., Gary, S. P., et al. 1995a, *SSRv*, **72**, 109
- Phillips, J. L., Feldman, W. C., Gosling, J. T., & Scime, E. E. 1995b, *AdSpR*, **16**, 95
- Pierrard, V., Lazar, M., Poedts, S., et al. 2016, *SoPh*, **291**, 2165
- Pilipp, W. G., Miggenrieder, H., Muhlhausen, K.-H., Rosenbauer, H., & Schwenn, R. 1990, *JGR*, **95**, 6305
- Pulupa, M., Bale, S. D., Badman, S. T., et al. 2020, *ApJS*, doi:10.3847/1538-4365/ab5dc0
- Pulupa, M., Bale, S. D., Bonnell, J. W., et al. 2017, *JGRA*, **122**, 2836
- Roberts, O. W., Narita, Y., Li, X., Escoubet, C. P., & Laakso, H. 2017, *JGRA*, **122**, 6940
- Šafránková, J., Němeček, Z., Němec, F., et al. 2015, *ApJ*, **803**, 107
- Salem, C., Bosqued, J.-M., Larson, D. E., et al. 2001, *JGR*, **106**, 21701
- Salem, C., Hoang, S., Issautier, K., Maksimovic, M., & Perche, C. 2003, *AdSpR*, **32**, 491
- Schippers, P., Moncuquet, M., Meyer-Vernet, N., & Lecacheux, A. 2013, *JGR*, **118**, 7170
- Schwadron, N. A., Goelzer, M. L., Smith, C. W., et al. 2014, *JGR*, **119**, 1486
- Scime, E. E., Littleton, J. E., Gary, S. P., Skoug, R., & Lin, N. 2001, *GeoRL*, **28**, 2169
- Scudder, J. D., & Olbert, S. 1979, *JGR*, **84**, 2755
- Shoub, E. C. 1983, *ApJ*, **266**, 339
- Sitenko, A. G. 1967, *Electromagnetic Fluctuations in Plasma* (San Diego, CA: Academic Press)
- Sittler, E. C., & Scudder, J. D. 1980, *JGR*, **85**, 5131
- Štverák, Š., Maksimovic, M., Trávníček, P. M., et al. 2009, *JGR*, **114**, A05104